Numerical simulations of bar formation in the Local Group

Ornela F. Marioni,[1,2,3]⋆ Mario G. Abadi, [1,3] Stefan Gottlöber, [4] Gustavo Yepes [5,6]

[1]*Instituto de Astronomía Teórica y Experimental, UNC-CONICET, Laprida 854, X5000BGR Córdoba, Argentina.*
[2]*Facultad de Matemática, Astronomía, Física y Computación, UNC, Av. Medina Allende s/n, X5000HUA Córdoba, Argentina.*
[3]*Observatorio Astronómico de Córdoba, Universidad Nacional de Córdoba, Laprida 854, X5000BGR Córdoba, Argentina.*
[4]*Leibniz-Institut für Astrophysik Potsdam (AIP), An der Sternwarte 16, D-14482 Potsdam, Germany.*
[5] *Departamento de Física Teórica, Módulo 8, Facultad de Ciencias, Universidad Autónoma de Madrid, E-28049 Madrid, Spain.*
[6] *CIAFF, Facultad de Ciencias, Universidad Autónoma de Madrid, E-28049 Madrid, Spain.*

ABSTRACT

More than 50 per cent of present-day massive disc galaxies show a rotating stellar bar. Their formation and dynamics have been widely studied both numerically and observationally. Although numerical simulations in the ΛCDM cosmological framework predict the formation of such stellar components, there seems to be a tension between theoretical and observational results. Simulated bars are typically larger in size and have slower pattern speed than observed ones. We study the formation and evolution of barred galaxies, using two ΛCDM zoom-in hydrodynamical simulations of the CLUES project that follow the evolution of a cosmological Local Group-like volume. We found that our simulated bars, at $z = 0$, are both shorter and faster rotators than previous ones found in other studies on cosmological simulations alleviating the tension mentioned above. These bars match the short tail-end of the observed bar length distribution. In agreement with previous numerical works, we find that bars form in those systems where the disc self-gravity is dominant over the dark matter halo, making them unstable against bar formation. Our bars developed in the last 3-4 Gyr until they achieve their current length and strength; as bars grow, their lengths increase while their rotation speeds decrease. Despite this slowdown, at redshift $z = 0$ their rotation speeds and size match well the observational data.

Key words: galaxies: evolution – galaxies: formation – galaxies: bar – galaxies: kinematics and dynamics – (galaxies:) Local Group – galaxies: spiral

1 INTRODUCTION

Barred galaxies constitute about two-thirds of the disc galaxy population observed in the Local Universe with approximately half of them showing evidence of a strong bar (Sellwood & Wilkinson 1993).

Bars are found to have different sizes and shapes. They vary from large structures that dominate the entire disc to small oval distortions in the inner regions of the galaxies.These structures play a significant role in galaxy evolution, particularly in the redistribution of angular momentum between the disc and the dark matter halo (Debattista & Sellwood 2000; Athanassoula 2003).

Roughly speaking, two main parameters are commonly defined in order to characterise bar properties: bar length and pattern speed. Bar lengths can range from $l_{bar} \sim 1$ kpc (called short bars) up to $l_{bar} \sim 10$ kpc (called long bars).

Bars are formed by instabilities in the disc. These instabili-

ties may be produced by internal mechanisms that act over long timescales, redistributing mass in the inner regions of the galaxy and, therefore, their angular momentum. Or they may also be produced by external processes, like mergers and flybys that can delay or advance the bar formation (Moetazedian & Just 2016; Zana et al. 2018).

Miller & Prendergast (1968) and Hockney & Hohl (1969) were the pioneers who ran N-body simulations of discs of collisionless particles. In their simulations, they found that it is easy to form unstable discs that form a bar over a dynamical time-scale. On the other hand, it is difficult to build perfect rotationally supported discs free from instabilities. Although the global instabilities explain well the bar structure formation, there is not yet a good understanding of stable discs.

To stabilise these fragile discs, avoiding bar formation, Ostriker & Peebles (1973) proposed the addition of a massive non-rotating spherical halo surrounding the disc. Further on Efstathiou et al. (1982) implemented this idea using live dark matter haloes.

Early analytical and numerical work by Weinberg (1985)

⋆ E-mail: ornela.marioni@unc.edu.ar

showed that bars suffer dynamical friction against their surrounding haloes, which slows them down between bar and halo has been further developed by Little & Carlberg (1991); Hernquist & Weinberg (1992); Sellwood & Debattista (2006); Weinberg & Katz (2007a,b) and Sellwood (2008), among others.

Many studies of idealised models have focused on the analysis of bar formation and evolution (Combes et al. 1990; Debattista & Sellwood 2000; Athanassoula & Misiriotis 2002). They find that, as bars develop, they slow down and grow longer and stronger. More recently, studies with hydrodynamical cosmological simulations have been performed, such as, Scannapieco & Athanassoula (2012); Okamoto et al. (2015); Algorry et al. (2017); Peschken & Łokas (2019). Their results are not in complete agreement with observations since most of these results find that bars are strongly braked throughout their evolution, resulting in slow bars not consistent with the observations.

A commonly used method to classify bars as fast or slow rotators is the ratio between the corotation radius and the bar length $\mathcal{R} = \mathrm{R_{corot}}/l_{\mathrm{bar}}$. The corotation radius is the radius where the angular velocity of a circular orbit equals the bar angular velocity $\Omega_{\mathrm{bar}} = \mathrm{V_c(R_{corot})}/\mathrm{R_{corot}}$. If $1.0 < \mathcal{R} < 1.4$, the bar is considered *fast*, on the other hand, if $R > 1.4$ then the bar is considered *slow*. Using theoretical arguments, Contopoulos (1980) shows that a bar should be always inside the corotation radius, and thus a bar with $\mathcal{R} < 1.0$ will be physically impossible. Many observational results have demonstrated that bars have $\mathcal{R} \approx 1.4$ (Corsini 2011; Aguerri et al. 2015; Font et al. 2017). Meanwhile, previous numerical results with cosmological simulations (Algorry et al. 2017; Peschken & Łokas 2019) have shown that bars slow down excessively, giving values of $\mathcal{R} \approx 3 - 4$. This issue has created a supposed conflict between the existence of fast bars in the ΛCDM paradigm, calling into question this concordance cosmological model. A recent exception is the work of Fragkoudi et al. (2021) who, using the Auriga simulations, has shown that fast rotating bars can form in the ΛCDM model in agreement with observational studies. Our zoom-in simulations allow us to study the short tail-end of observational bars in complement with this previous work.

This paper is organised as follows: in Section 2 we present the simulations analysed in this work and the sample selected. In Section 3, we show the main properties of the bars: bar strength, bar length and pattern speed, and comment on the main results. In Section 4, we include the summary and conclusions of our work.

2   SIMULATIONS

We analyse two sets of simulated galaxies from two zoom-in high-resolution simulations that are part of the CLUES-project [1] (Gottlöber et al. 2010; Yepes et al. 2014). This collaboration aims to run N-body plus hydrodynamical cosmological simulations, mimicking the observational properties of the Local Group of galaxies. Observational data is used to constrain initial conditions to resemble the final mass distribution and velocity field of the Local Group. These observational constraints are set up from peculiar velocities from the MARK III (Willick et al. 1997), surface brightness fluctuations from Tonry et al. (2001), the catalogue of neighbouring galaxies (Karachentsev et al. 2004) and the catalogue of nearby X-ray selected clusters of galaxies (Reiprich & Böhringer 2002). Then, the

----

[1] Constrained Local UniversE Simulations:
https://www.clues-project.org/cms/

Table 1. Final ($z = 0$) simulation parameters of the high-resolution region. In column (1) we have the simulation code. Then in columns (2), (3) and (4) are the dark matter, gas and star particles masses, and in columns (5) and (6) there are the softening radius of dark matter ϵ_{DM} and baryon ϵ_{BAR} particles respectively.

Simulation code	$\mathrm{m_{DM}}$ [$10^5 \mathrm{M}_\odot$]	$\mathrm{m_{GAS}}$ [$10^4 \mathrm{M}_\odot$]	$\mathrm{m_{STR}}$ [$10^4 \mathrm{M}_\odot$]	ϵ_{DM} [kpc]	ϵ_{BAR} [kpc]
GADGET-2	2.87	6.06	3.02	0.14	0.14
GASOLINE	2.87	6.06	1.45	0.49	0.22

initial conditions are generated as constrained realisations of Gaussian fields employing the Hoffman & Ribak (1991) algorithm in a 256^3 uniform mesh. Even though the initial conditions of the simulations are designed to reproduce the large-scale environment of the Local Group, at smaller scales ($\lesssim 1h^{-1}$ Mpc) they remain mainly random. Therefore, several runs have been made to obtain the correct Local Group candidate (i.e. two haloes located at a proper distance with their correct relative velocities, masses, etc.)

These initial conditions are used to first run a cosmological dark matter-only simulation in a box of $64h^{-1}$ Mpc size with 1024^3 particles with cosmological parameters ($\Omega_\Lambda = 0.76$, $\Omega_m = 0.24$, $\Omega_b = 0.042$, $h = 0.73$, $\sigma_8 = 0.75$ and $n = 0.95$) given by WMAP3 (Spergel et al. 2007). Then, a smaller approximately spherical region of $2h^{-1}$ Mpc radius is re-simulated at a higher resolution using the Klypin et al. (2001) zoom-in technique with 4096^3 effective dark matter-particles adding the same number of gas particles. This region is selected, at redshift $z = 0$, in the original box to enclose the three most massive dark matter haloes at the position of the Local Group candidate.

Both zoom-in simulations start from the same initial conditions but are evolved with two different hydrodynamical codes: TreePM+SPH GADGET-2 code (Springel 2005) and N-body+SPH GASOLINE code (Wadsley et al. 2004).

The CLUES-GADGET2 simulation follows radiative cooling, star formation, supernova feedback, etc. as described by Springel & Hernquist (2003). The interstellar medium is modelled as a two-phase medium composed of hot and cold gas affected after redshift $z = 6$ by an uniform but evolving cosmic ionising ultraviolet background (Haardt & Madau 1996). Cooling is independent of the medium metallicity and there is no cooling below 10^4 K. The gas is enriched by supernova explosions. Gas particles spawn into stars when they reach certain conditions. Each gas particle can spawn on two star particles only. When the first star is born, it has half the mass of its progenitor gas particle and this particle loses half of its mass. When the second star is born, the progenitor disappears to preserve the total mass. Star particles interact with other particles in the same way as dark matter particles do (i.e., as collisionless particles), and only a small fraction $\beta = 0.12$ will explode as supernovae. The CLUES-GADGET2 simulation has been described in more detail by Libeskind et al. (2010). It has also been analysed in several other works, e.g. Libeskind et al. (2011); Knebe et al. (2011); Benítez-Llambay et al. (2013, 2015).

The CLUES-GASOLINE simulation uses the physics implemented in Governato et al. (2010) and Guedes et al. (2011). It includes star formation, gas cooling, supernova feedback and a cosmic ultraviolet background of Haardt & Madau (1996). Star formation proceeds differently from the other simulation. When the gas becomes cold and dense, star formation can take place following the Schmidt law with a star formation rate $\propto \rho^{1.5}$. When these stars die, they enrich the interstellar medium with metals, and the returned gas has the same metallicity as the dead star. Energy feed-

Table 2. Main properties of simulated galaxies. From left to right: virial mass, stellar mass, virial radius, half mass (stellar) radius, bar length, bar pattern speed, corotation radius, quotient between the mean corotation radius and mean bar length, bar formation time.

Galaxy name	M_{vir} $[10^{11}M_\odot]$	$M_{stellar}$ $[10^{10}M_\odot]$	r_{vir} [kpc]	r_{50} [kpc]	l_{bar} [kpc]	Ω_{bar} [km s^{-1}kpc^{-1}]	R_{corot} [kpc]	$\bar{\mathcal{R}}$	t_{bar} [Gyr]
A-Gadget2	6.15	1.33	167.2	1.61	$1.40^{+0.13}_{-0.14}$	$71.43^{+3.75}_{-2.57}$	$2.13^{+0.06}_{-0.09}$	1.52	8.68
A-Gasoline	5.93	1.11	166.8	0.87	$0.90^{+0.02}_{-0.01}$	$99.16^{+3.20}_{-6.13}$	$1.59^{+0.09}_{-0.05}$	1.76	8.09
B-Gadget2	4.69	1.38	153.5	2.40	-	-	-	-	-
B-Gasoline	4.59	1.03	150.5	2.24	$1.45^{+0.37}_{-0.24}$	$32.67^{+0.48}_{-0.85}$	$3.79^{+0.10}_{-0.06}$	2.61	10.62
C-Gadget2	2.36	0.79	123.1	3.74	-	-	-	-	-
C-Gasoline	2.28	0.48	119.6	2.58	-	-	-	-	-

back is implemented following Stinson et al. (2006). The number of stars that explode as supernovae and their total mass are obtained from stellar lifetime calculations from Raiteri et al. (1996). The CLUES-GASOLINE simulation has been described in more detail by Santos-Santos et al. (2016). It has also been analysed in Santos-Santos et al. (2017) and Mostoghiu et al. (2018).

In Table 1, we list the final ($z = 0$) particle masses and softening lengths of each high-resolution simulation. Note that the difference in stellar masses is due to the different physical processes of star formation that each simulation uses. For CLUES-GADGET2 simulation, all stellar particles have the same mass, half that of the gas particle. Meanwhile, in the CLUES-GASOLINE simulation, stellar particles have different masses, in this case, we quote in Table 1 the median of the masses. The softening radius is fixed in comoving coordinates in the CLUES-GASOLINE simulation, while, in the CLUES-GADGET2 simulation, it is comoving until $z = 4$ and then remains fixed in physical coordinates. We have confirmed that all the distances that we are dealing with are longer than the softening radius for all redshifts.

For both simulations, haloes have been identified using the MPI+OpenMP hybrid halo finder AHF (Knollmann & Knebe 2009). This implementation places overdensities in an adaptive smoothed density field as probable halo centres. For each overdensity, the potential minimum is calculated and the gravitational bound particles are determined. Only the peaks with $\gtrsim 20$ particles are considered haloes that will be studied later. This algorithm identifies hierarchical substructures automatically as haloes, subhaloes, sub-subhaloes, etc. A subhalo is defined as a halo that lives in a more massive halo. The merger tree was built following the ten most bound particles of each halo back through the snapshots, and associating these particles to the nearest halo centre.

2.1 Galaxy sample

At redshift $z = 0$, we select the three most massive haloes (named A, B and C) identified in each simulation (CLUES-GADGET2 or CLUES-GASOLINE). We check that these haloes are free from contaminating low-res dark matter particles. We list the main properties of these galaxies in Table 2. Virial radius r_{vir} is defined as the radius where the average integrated mass density is $\Delta = 200$ times the critical density of the Universe and virial mass M_{vir} is the total mass inside r_{vir}. Following Sales et al. (2010, see also Benítez-Llambay et al. (2013, 2015); Ferrero et al. (2017)) we define the galaxy radius r_{gal} as $0.15r_{vir}$; this is the radius that includes most of the stellar particles contained inside the dark matter halo ($\gtrsim 85\%$ in our galaxies) and there is no substructure inside; i.e., no subhalo is found by the AHF algorithm inside the galaxy radius. Stellar mass $M_{stellar}$ is computed inside a sphere of radius r_{gal}. The half-mass radius r_{50} is the radius enclosing half of the stellar mass.

It should be noted that these three main galaxies and their cor-

responding dark matter haloes are systematically less massive (by a factor 2-3 in virial mass and by a factor 5-7 in stellar mass) than the current estimates of the masses of the three main spiral galaxies of our Local Group (namely Andromeda, Milky Way and Triangulum). However, they do fit (Benítez-Llambay et al. 2013) the abundance matching relation (Guo et al. 2010) and can be considered as normal disc-like galaxies suitable for analysing the formation of barred stellar components in this cosmological context. We would like to point out that a comparison between simulations is beyond the scope of this paper. Each galaxy is analysed as an individual system. However, it should be noted that these galaxies cannot be used as an independent sample because they are generated using the same initial conditions.

3 ANALYSIS AND RESULTS

Fig. 1 shows, at redshift $z = 0$, face-on (left panels) and edge-on (right panels), the projected stellar mass density distribution Σ of our six simulated galaxies (see labels) in a box of side 10 kpc. Images were generated using the package Py-SPHViewer (Benitez-Llambay 2015), coloured according to their projected stellar mass density using a logarithmic scale, and rotated to have the total stellar angular momentum aligned with the z-axis.

Visual inspection of these figures shows that at least three of the studied galaxies present an elongate structure in the centre.

3.1 Bar properties

Following Athanassoula et al. (2013) we identify bars in our simulated galaxies, computing the amplitudes through the $m = 2$ Fourier modes of the face-on projected stellar mass distribution (Fig. 1, left panels), defined as follows:

$$a_2(R) = \frac{1}{M(R)} \sum_{i=1}^{N(R)} M_i \, cos(2\phi_i)$$
$$b_2(R) = \frac{1}{M(R)} \sum_{i=1}^{N(R)} M_i \, sin(2\phi_i). \tag{1}$$

Here, R is the cylindrical radius of a ring defined by distances in the range $[R, R + dR]$, ϕ_i and M_i are the azimuthal angle and the stellar mass of the ith particle inside the ring, respectively; $N(R)$ is the number of particles within the ring and $M(R) = \sum_{i=0}^{N(R)} M_i$ its corresponding mass. Then, the bar strength can be quantified through the normalised amplitude of the $m = 2$ mode:
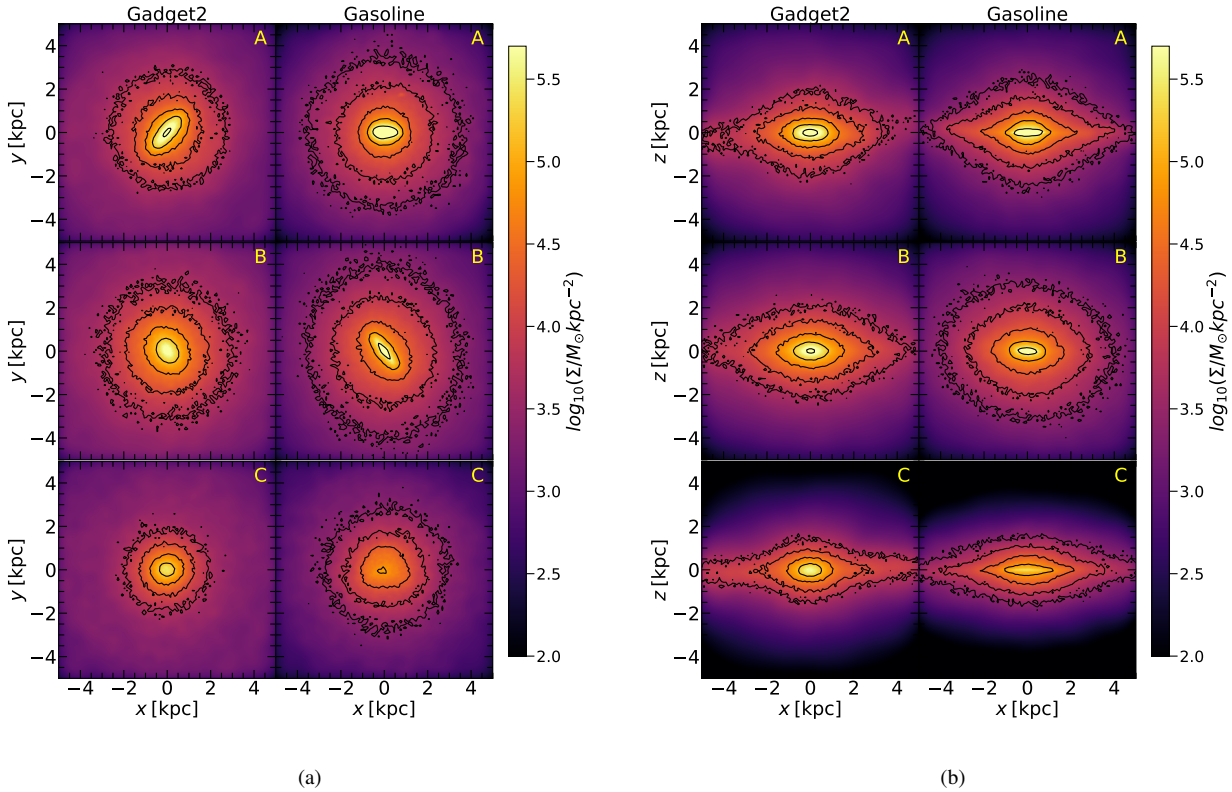
$$A_2(R) = \sqrt{a_2^2(R) + b_2^2(R)} \tag{2}$$

Figure 1. Projected stellar mass density Σ: (a) face-on and (b) edge-on views at redshift $z = 0$ of the central regions of the galaxies in a box of side $10\,\mathrm{kpc}$. On the left of each figure, there are galaxies of CLUES-GADGET2 and on the right, galaxies of CLUES-GASOLINE. The solid lines correspond to five density isocontours chosen arbitrarily at $log_{10}(\Sigma) = 3.3, 3.7, 4.2, 4.7$ and 5.5.

With this definition, for a perfectly aligned distribution, as in a bar, $A_2 = 1$ given that $a_2 = \int_0^{2\pi} \cos(2\phi)d\phi = \cos(2\phi_0)$ and $b_2 = \int_0^{2\pi} \sin(2\phi)d\phi = \sin(2\phi_0)$, where ϕ_0 is the bar position angle.

In Fig. 2, we show the bar strength parameter $A_2(R)$ (top panel) for our six simulated galaxies, computed in 20 cylindrical equal-number bins[2] in the range $0 < R < 6\,\mathrm{kpc}$. This means between $\sim 8,000$ particles per bin for the less massive galaxy, and up to $\sim 32,000$ for the most massive one.

In the top panel of Fig. 2 we can see three high peaks; galaxies A-Gadget2, A-Gasoline and B-Gasoline, with a radial profile with a maximum of $A_2 > 0.4$ in their central regions, while the remaining three galaxies (B-Gadget2, C-Gadget2 and C-Gasoline) show a relatively flat profile with $A_2 < 0.1$.

Following Algorry et al. (2017), we classify galaxies as barred or unbarred based on the $A_2(R)$ maximum value A_2^{max}; if $0 < A_2^{\mathrm{max}} < 0.2$, the galaxy is classified as unbarred, while if $0.2 < A_2^{\mathrm{max}} < 1.0$, it is a (weakly or strongly) barred galaxy. Thus, A-Gadget2, A-Gasoline and B-Gasoline are barred galaxies and B-Gadget2, C-Gadget2 and C-Gasoline are unbarred, which we confirmed previously by visual inspection of the face-on projections of stellar mass density (Fig. 1(a)).

---

[2] The bins are built in order that each bin contains the same number of particles.

3.1.1 Determination of bar length

Bar length l_{bar} is one of the most important properties of barred galaxies. There is no single way to define the length of a bar; Athanassoula & Misiriotis (2002) present a compilation of different methods to estimate bar length. Scannapieco & Athanassoula (2012) implemented some of these methods in cosmological numerical simulations, showing general agreement between them. In this work, we have used four different methods to estimate bar length: the three methods used in Scannapieco & Athanassoula (2012) plus the method implemented by Algorry et al. (2017).

- *method 1*: following Algorry et al. (2017), the first method consists in estimating the bar length on the $A_2(R)$ profile where the curve drops below 0.15 after reaching its maximum (A_2^{max}).

- *method 2*: the second method is similar to the first; instead of using a fixed threshold for all galaxies, it uses a fraction of the maximum value (A_2^{max}). In theory, if the disc and the bar were rigid bodies, the bar length would be the radius where the $A_2(R)$ profile drops to zero. However, this does not occur in simulated galaxies; therefore, we must choose this value arbitrarily. Following Scannapieco & Athanassoula (2012), we choose this value as 25% of the A_2^{max}.

- *method 3*: the third method uses the azimuthal angle radial profile $\phi(R)$ to estimate bar length. The azimuthal angle is calculated from the face-on projected mass distribution (Eq. 1), where $\phi(R) = 0.5 \arctan(b_2/a_2)$. Theoretically, if we consider the bar as a solid body, the position angle of the bi-dimensional mass distri-
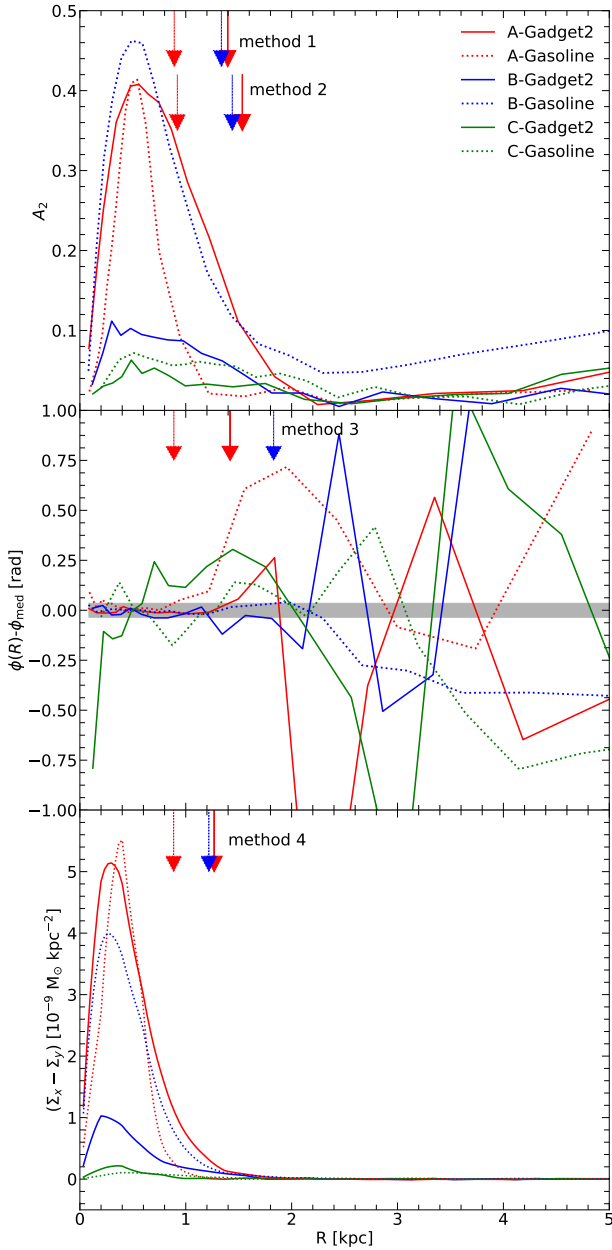
Figure 2. Top: normalised Fourier amplitude of the bi-dimensional mass distribution (A_2) of the central region of galaxies in function of the cylindrical radius (R). Middle: phase of the stellar bi-dimensional mass distribution scaled by a mean phase value $\phi(R) - \phi_{\mathrm{med}}$ in function of the cylindrical radius (R). ϕ_{med} is taken as an average of the bar phase at the radius where the A_2 profile peaks with the two previous and two following bins values. The shadowed region corresponds to the chosen threshold ($\pm 2°$). Bottom: difference of the surface stellar density between semi-major and semi-minor axis of the central mass distribution of the galaxies. If the central region is axisymmetric, the difference is close to zero. The arrows on the top of the panels show the bar length measured with the different methods. CLUES-GADGET2 galaxies are plotted with coloured solid lines and CLUES-GASOLINE galaxies are plotted with coloured dotted lines. We choose red, blue and green for galaxies A, B and C, respectively.

Table 3. Values of bar length at $z = 0$ in units of kpc measured with the different methods.

	A-Gadget2	A-Gasoline	B-Gasoline
method 1	1.40	0.89	1.34
method 2	1.53	0.92	1.44
method 3	1.42	0.89	1.83
method 4	1.27	0.89	1.22

bution should be constant along the bar. This is not completely true for simulations or observations, as the phase of the bar varies little along the bar, so the phase can be considered within a certain tolerance threshold. Athanassoula & Misiriotis (2002) and Scannapieco & Athanassoula (2012) use a threshold of $\pm arcsin(0.3)$, which is chosen ad hoc. We chose a smaller threshold ($\pm arcsin(0.035)$) to improve the quality of the bar length determination. As seen in the middle panel of Fig. 2, the first large fluctuations of the bar phase determine the bar size. Looking at the curves, at small radii ($R \lesssim 1.5\,\mathrm{kpc}$) the bar position angle is almost constant with very small fluctuations contained inside the grey shaded area. At large radii ($R \gtrsim 1.5\,\mathrm{kpc}$) the fluctuations increase their amplitude considerably. Such large oscillations indicate that the position angle of the bar is not well defined and point out that the bar has ended and the disc is the dominant component.

- *method 4*: The fourth method estimates the bar length using the difference between stellar density profiles along semi-major and semi-minor axes of the bar. In the centre of the galaxies, the density profile along both axes must coincide and, as we move along the bar, the difference between these profiles must be increasing. Where the bar ends, these profiles must be equal again (if we consider an axisymmetric disc). This theoretical argument is not completely valid in cosmological simulations. The profiles will tend to approximate each other but they never will be equal. Following Scannapieco & Athanassoula (2012), we take the bar length as the radius where the difference between the profiles drops to 5% of their maximum value.

The resulting bar length measurements are marked with coloured arrows in Fig. 2. The bar length values are also quoted in Table 3. Table 2 lists the mean values of bar length as the average of the four methods. The errors of bar length are the maximum difference between each method to the mean value. We can see from Table 3 that all the values are in good agreement. It should be noted that the method that results in a shorter (or longer) bar length estimation, does not necessarily result in a shorter (or longer) bar length estimation in another galaxy too.

3.1.2 Pattern speed estimation

Another characteristic property of bars is the pattern speed Ω_{bar}. The pattern speed determines how fast the bar rotates. Theoretically, the bar should behave as a solid body, but in practice this is not true. There are many contaminating particles from the disc and the bulge. To avoid this kind of particle, we have taken the pattern speed averaging the angular velocity $\Omega(R) = V_\phi/R = (xv_y - yv_x)/(x^2 + y^2)$ of star particles at the extremes of the bar: $l_{\mathrm{bar}} \pm 0.15\,\mathrm{kpc}$, $\phi_{\mathrm{med}} \pm 5°$ and $z \pm 1\,\mathrm{kpc}$. Since we have four values for l_{bar} from the different methods, we calculate Ω_{bar} for each bar length and average them. We take the errors as the maximum absolute difference between the individual pattern speed and the mean value. The values of Ω_{bar} are shown in Table 2.

In Fig. 3, we plot Ω_{bar} as a function of the bar length l_{bar} for our three barred galaxies (coloured diamonds) and compare them
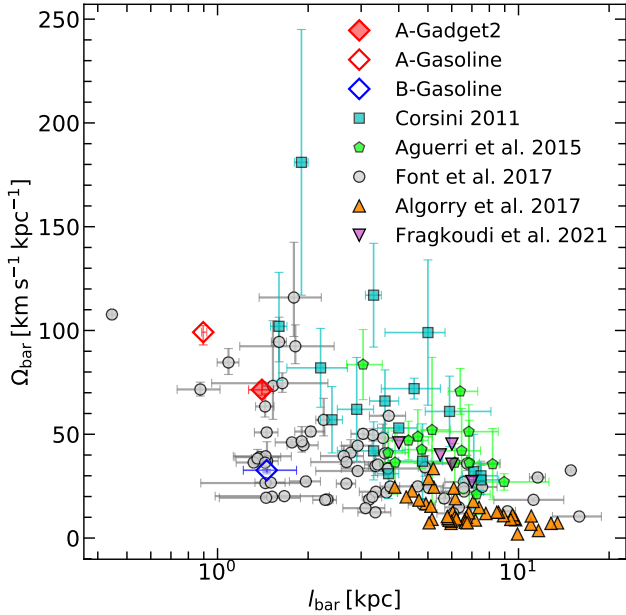
Figure 3. Pattern speed of the barred galaxies Ω_{bar} as function of the bar length l_{bar}. The coloured diamonds show the mean of the four values of Ω_{bar} and l_{bar} estimations for our simulated galaxies. The error bars show the maximum difference between the mean and the four measurements. Grey circles shows observational data of Font et al. (2017), green pentagons are galaxies from Aguerri et al. (2015), cyan squares are galaxies from Corsini (2011), orange triangles are galaxies of EAGLE simulations from Algorry et al. (2017), pink inverted triangles are galaxies of AURIGA simulations from the work of Fragkoudi et al. (2021).

Figure 4. Corotation radius R_{corot} as function of bar length l_{bar}. The diamonds show the mean of the four values of R_{corot} and l_{bar} estimations and the error bars show the maximum difference between the mean and the four measurements. See labels on the plot. The dashed line represents the correlation $R_{corot} = 1.4 l_{bar}$ that divides the barred galaxies into slow and fast rotators.

with observational results from Font et al. (2017); Aguerri et al. (2015) and Corsini (2011). We also compare them to the theoretical predictions of Algorry et al. (2017) and Fragkoudi et al. (2021) for barred galaxies in the EAGLE and AURIGA simulations respectively. This figure shows that our simulated bars occupy the short tail-end of l_{bar} in the observed bar length distribution, contrary to earlier claims that simulations often produce long bars but rarely short ones (Erwin 2005). They are also systematically shorter by a factor ~ 5 than the typical values obtained in the EAGLE or AURIGA cosmological simulations (Algorry et al. 2017; Fragkoudi et al. 2021). It also shows that the pattern speeds are in good agreement with the range obtained from observational results of Font et al. (2017), with A-Gadget2 and A-Gasoline galaxies rotating fast and B-Gasoline rotating at a much slower rate.

As seen in Fig. 3 rotation speeds depend on the bar length and so, to know if a bar is rotating fast or slow according to its length, Ω_{bar} is usually expressed in terms of the quotient of the corotation radius R_{corot} and the bar length l_{bar}. In Fig. 4, we plot the corotation radius R_{corot} as a function of bar length l_{bar} using the same symbol and colour coding as in Fig. 3. As for Ω_{bar}, we calculate four values for the corotation radius and take the average as the R_{corot} for each galaxy. The error bars correspond to the maximum difference between each measurement and the mean. The dashed line shows the relation $R_{corot} = 1.4 l_{bar}$, which is usually implemented to classify bars as *slow* or *fast* rotators (Debattista & Sellwood 2000). In this plot, we can see that our simulated bars fit the short tail-end of fast bars, complementing the results from Fragkoudi et al. (2021) and in good agreement with observational data.
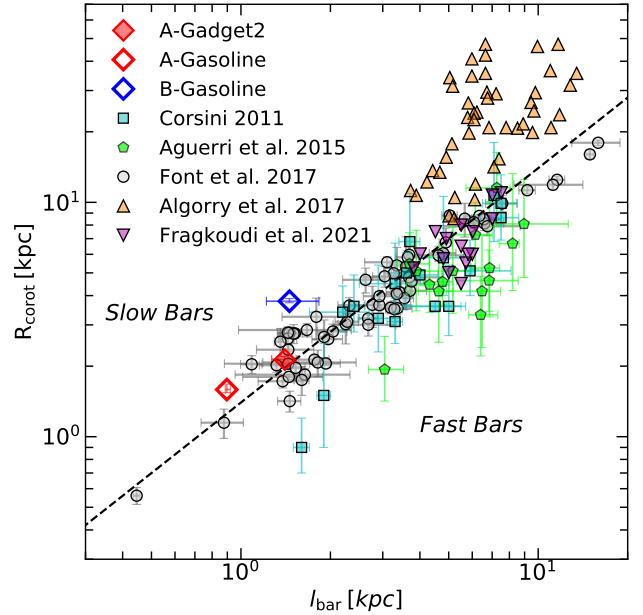
3.2 Bar temporal evolution

3.2.1 Onset of the bar

As well as measuring the bar strength at $z = 0$ to determine the bar presence, we can analyse its evolution to estimate the bar formation time (see Fig.5). Although bar formation is a process rather than an event, during a galaxy's lifetime a characteristic time of bar formation can be defined using these curves. Following Algorry et al. (2017), we define the bar formation time t_{bar} as the time when the bar strength parameter crosses the threshold $A_2^{max} = 0.2$ for the last time bottom up. In the practice, we select bars at $z = 0$, follow these bars back in time and see the last time when the A_2^{max} parameter crossed the 0.2 threshold and select this time as the bar time formation t_{bar}. In Fig. 5, we show the bar strength parameter in function of time for our simulated galaxies. At early times, A_2^{max} parameter shows a noisy behaviour, because of mergers and the fly bys that the galaxy suffers during its formation. After this period, the strength parameter shows a rising profile for barred galaxies, but remains approximately constant for unbarred ones.

Vertical arrows show $t_{bar} = 8.69$, 8.09 and 10.62 Gyr for A-Gadget2, A-Gasoline and B-Gasoline respectively, while for the three unbarred galaxies, at late times ($t \gtrsim 8$ Gyr), A_2^{max} are always below the 0.2 limit. The three bars develop in the last 3-6 Gyr after the accretion epoch. The bar of A-GASOLINE grows rapidly (~ 1 Gyr), while the bars of A-GADGET and B-GASOLINE take longer (~ 4 Gyr and ~ 3 Gyr respectively) to reach their maximum strength. Once the bar strength reaches its maximum, it remains approximately constant up to the present.
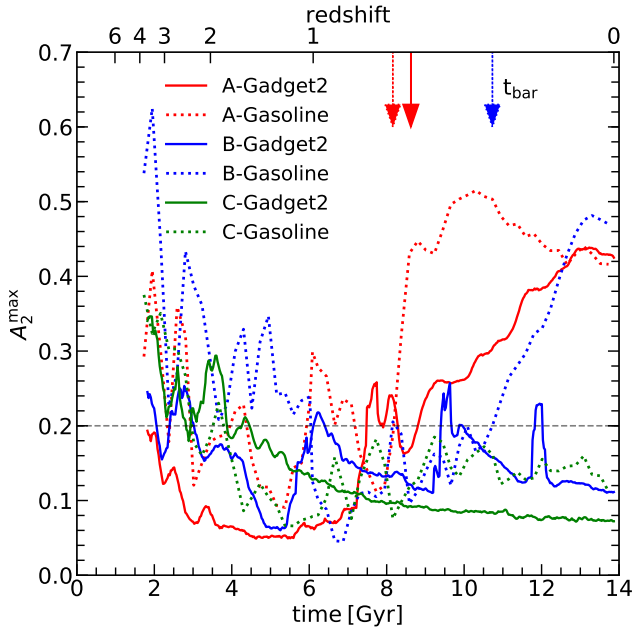
Figure 5. Bar strength A_2^{max} as a function of time. We use the same colour coding as Fig. 2. We consider that a galaxy has a bar when the A_2^{max} parameter exceeds the limit of $A_2^{max} = 0.2$ (grey dashed horizontal line). The arrows on the top of the plot show the time at which the A_2^{max} parameter crosses the grey dashed line for the last time (bottom up); therefore, we take this time as the bar formation time t_{bar}. Note that a running average algorithm has been applied to smooth the curves.

3.2.2 *Analysing disc instability*

Early numerical simulations of self-gravitating cold discs have shown that they become rapidly unstable against bar formation (Miller & Prendergast 1968; Hockney & Hohl 1969; Miller et al. 1970; Kalnajs 1972; James & Sellwood 1978; Combes & Sanders 1981; Sparke & Sellwood 1987, among others). Ostriker & Peebles (1973) and Efstathiou et al. (1982) implemented dark matter halos to stabilise these discs, proposing that bars form in stellar discs where self-gravity makes the dominant contribution while unbarred discs are those where the dark matter prevails. They also introduced the ratio between the maximum rotational velocity and the individual disc contribution as a parameter to predict the stability of cold discs.

Accordingly, semi-analytical models of galaxy formation (e.g. Mo et al. 1998; Cole et al. 2000; Bower et al. 2006; Lacey et al. 2016) usually implement a slightly modified version of this parameter as the ratio between total and disc circular velocities (both at the half-mass radius) as a bar-instability parameter that makes it possible to distinguish between stable and unstable discs:

$$f_{disc} = \frac{V_c(r_{50})}{\sqrt{GM_{disc}/r_{50}}}. \tag{3}$$

In our work, we use the version used by Algorry et al. (2017) applied in EAGLE simulations. In Eq. 3, $V_c(r_{50})$, is the total circular velocity of the galaxy at the half stellar-mass radius (r_{50}), G is the gravitational constant and M_{disc} is the galaxy stellar mass. We confirm by a double exponential fit that our galaxies are in fact disc galaxies in order to perform this approximation. Systems with $f_{disc} \lesssim 1.1$ are considered to have gravitationally unstable discs,
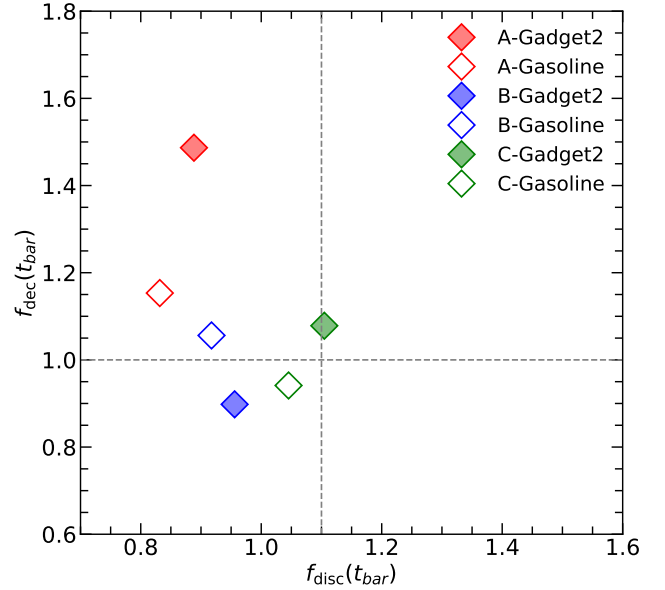

Figure 6. f_{dec} vs f_{disc} parameters. Each parameter is measured at the bar formation time t_{bar}. Following Algorry et al. (2017), for unbarred galaxies we have taken $t = 8.8$ Gyr ($z = 0.5$). Horizontal and vertical dashed lines indicate the values $f_{dec} = 1.0$ and $f_{disc} = 1.1$ thresholds respectively.

while those with $f_{disc} \gtrsim 1.1$ are stable without developing a barred structure.

While the f_{disc} parameter seems to be a good predictor of disc instability, there is evidence that this parameter alone is insufficient to predict bar formation (Athanassoula 2008). Numerical simulations have shown that initially *stable* discs ($f_{disc} \gtrsim 1.1$) can develop a bar (Athanassoula & Misiriotis 2002; Athanassoula 2003), and even if a disc is *bar unstable* ($f_{disc} \lesssim 1.1$), a bar may not develop because of high velocity dispersion of the dark matter halo. To solve this issue, Algorry et al. (2017) proposed combining the f_{disc} parameter with another parameter that takes into account the global importance of the whole system and not only the local gravitational importance of the disc:

$$f_{dec} = \frac{V_c(r_{50})}{V_{max,halo}}. \tag{4}$$

The f_{dec} parameter measures the decline in the curve of total circular velocity, where $V_c(r_{50})$ is the total circular velocity of the galaxy at the half stellar-mass radius and $V_{max,halo}$ is the maximum circular velocity of the dark matter halo. Thus a galaxy with $f_{dec} < 1$ is a galaxy whose circular velocity increases beyond that of the disc, in such a way that the velocities of the halo particles will be higher than those of the disc, which may prevent the assembling of the particles on the bar delaying its formation or avoiding it completely. Galaxies with $f_{dec} > 1$ are those with declining rotation curves, where the rotation velocity of the disc predominates over the velocity of halo particles. Then, we adopt $f_{dec} = 1$ as the threshold to divide between favoured ($f_{dec} > 1$) and disfavoured ($f_{dec} < 1$) galaxies for bar formation.

In Fig. 6, we show the f_{dec} vs f_{disc} parameters, both calculated at bar formation time t_{bar}. We see that barred galaxies locate in the top left quadrant of the plot, i.e. although each parameter separately is not a good predictor of disc instability, if we combine both
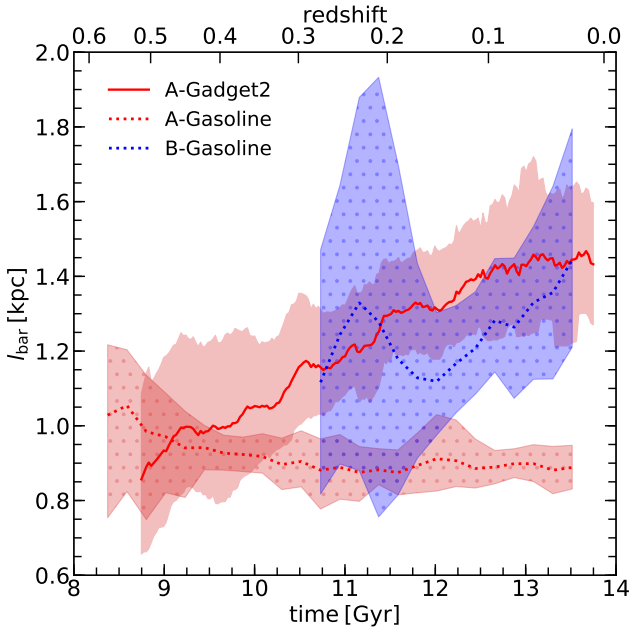
Figure 7. Bar length as a function of time. The curves start at the bar formation time t_{bar}

of each galaxy (see Fig. 5). Galaxies A-Gadget2, A-Gasoline, B-Gasoline are plotted with red solid, red dotted and blue dotted lines respectively. Each curve corresponds to the mean l_{bar} estimation. The shaded regions show the maximum difference in bar length between the four methods and the mean. Note that a running average algorithm has been applied to smooth the curves.

parameters, we obtain a good prediction method for *bar unstable* galaxies.

This analysis could explain why even if we have pairs of galaxies obtained from the same initial conditions, one has a bar (B-GASOLINE) and the other does not (B-GADGET2). Similarly, it helps to understand why C-GADGET2, despite having twice the stellar mass of C-GASOLINE, does not develop a bar even though both have similar haloes. We expand this discussion at the end of Section 3.3.

3.2.3 *Bar length and pattern speed evolution*

Previous works (e.g. Debattista & Sellwood 2000; Athanassoula & Misiriotis 2002) have shown that as a bar develops, it grows and slows down. We examine this behaviour in Fig. 7, where we plot the temporal evolution of bar length as a function of cosmic time for our three barred galaxies, starting from their formation time (t_{bar}) all the way to redshift $z = 0$. In this figure, we can see that galaxies A-Gadget2 and B-Gasoline increase their length by a factor of 1.3 and 1.7, respectively, while for A-Gasoline, it is fixed almost at a constant value. Bar growth is accompanied by a consistent slowing down of the pattern speed, as we can see in Fig. 8. In this figure, for galaxies A-Gadget2 and B-Gasoline, we see a decreasing pattern speed for a factor of 0.7 and 0.4, respectively, while for A-Gasoline the evolution of Ω_{bar} is nearly flat.

The temporal evolution of the bar length and pattern speed seems to correspond with the evolution of the bar strength (A_2^{max}, see Fig. 5). After the bar formation time (t_{bar}), A_2^{max} grows with an approximately constant slope for galaxies A-Gadget2 and B-
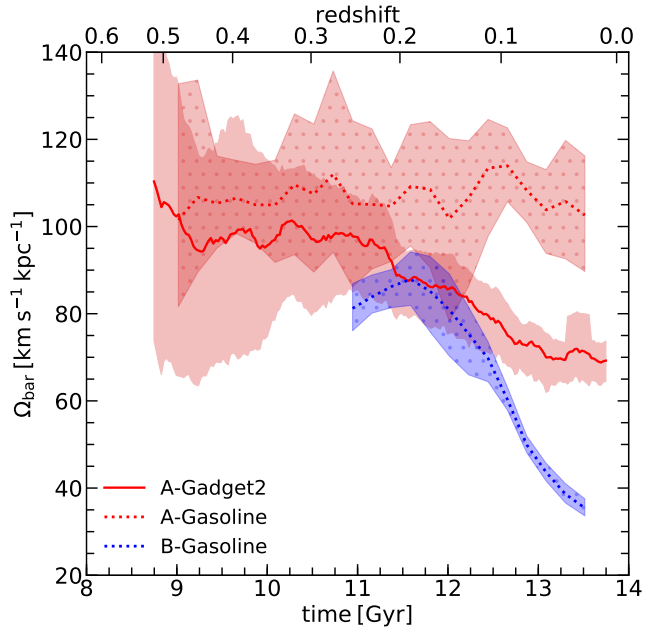

Figure 8. Pattern speed of the bar as a function of time. The curves represent the mean Ω_{bar} of each galaxy between the four estimations of bar length. The shaded region represents the maximum difference between the four measurements of pattern speed for the different estimations of bar length and the mean. Each curve starts at the bar formation time (see Fig. 5). The same colour coding as Fig. 7 is used. Here we also applied a running average algorithm to smooth the curves.

Gasoline although slightly steeper for B-Gasoline. For A-Gasoline, after t_{bar}, the A_2^{max} parameter increases rapidly reaching a maximum value and then decreases by only a factor of $\sim 20\%$. An analogue behaviour is seen in the bar length evolution (Fig. 7) in which both A-Gadget2 and B-Gasoline show a positive slope while A-Gasoline is approximately constant.

3.3 Formation time of stellar particles forming the bar

In this section, we analyse the star formation history of the galaxies. In Fig. 9 we plot the distance d of star particles from the galaxy centre at their formation time as a function of this time for those stars that belong to the galaxy at redshift $z = 0$. We classify stars as born *in-situ* or *accreted*, according to their distance from the centre of the galaxy at the moment of their formation. Distances range between $0 \lesssim d \lesssim 400\,\mathrm{kpc}$ for all star particles that, at redshift $z = 0$, belong to the galaxy $r < r_{gal}$ (black dots), or those that belong to the bar (orange dots). The horizontal grey dashed line shows our threshold for classifying stars as *in-situ* ($d < 15\,\mathrm{kpc}$) or *accreted* ($d > 15\,\mathrm{kpc}$). Stars that belong to the bar are defined as those inside a triaxial ellipsoid with semi-axis ratios given by the shape tensor ($T_{ij} = \sum_{k=1}^{N} x_i x_j$ with i and j being the corresponding permutations between x, y and z coordinates and N the total number of particles) computed using all star particles inside the bar length $r < l_{bar}$. Through this procedure, we find that a significant fraction, about 43%, 44% and 35% of stars belong to the bar for galaxies A-Gadget2, A-Gasoline and B-Gasoline, respectively. These fractions correspond to a stellar mass $M_{stellar} \sim 10^{10}\,M_\odot$, which is very close to the mean stellar mass of the Font et al. (2017) sample.

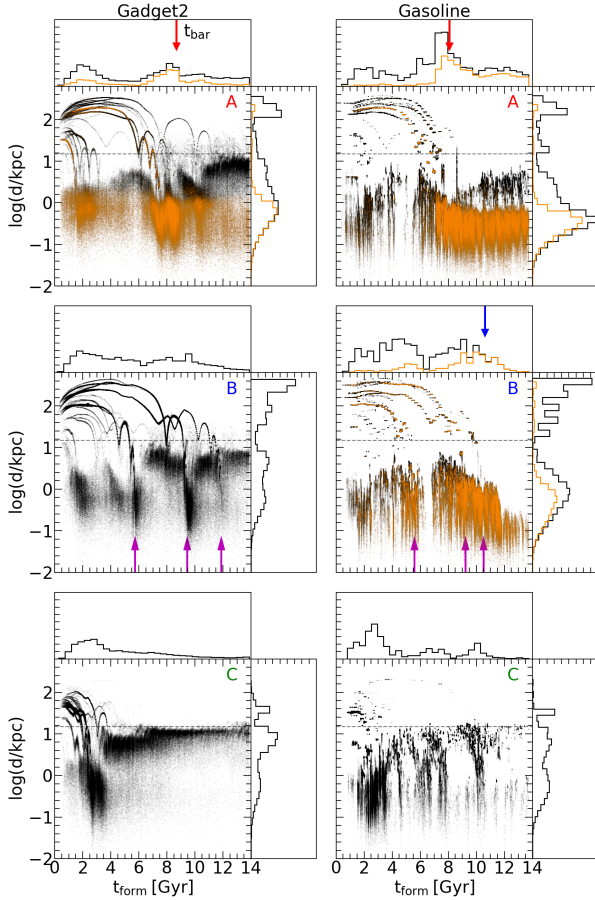As expected for disc-like galaxies, most stars are born *in-*

Figure 9. Distance of the stars to the centre of the galaxy at their formation time as a function of that time. The black dots show the total stars inside the galaxy radius and the orange dots show the stars that belong to the bar at $z = 0$. The grey dashed horizontal line shows our division between *in-situ* ($d < 15$ kpc) and *accreted* ($d > 15$ kpc) stars. The upper and right histograms are the distribution of both variables. Each tick mark of the histograms correspond to 10^4 counts, the maximum being 90,000 counts. The vertical arrows at the top indicate the formation time of the bar t_{bar} (see Fig. 5 and Table 2), which coincides with the peak of star formation in the galaxy. Vertical magenta arrows in middle panels indicate the time of the merger events of B-galaxies.

situ, with fractions of 72%, 47% and 81% for galaxies A, B and C of CLUES-GADGET2 simulation respectively and 78%, 56% and 86% for galaxies A, B, C of CLUES-GASOLINE simulation, respectively. Fluctuations in these fractions between the CLUES-GADGET2 and CLUES-GASOLINE runs of each galaxy are ∼ 10%. However, if we focus only on the stars that belong to the stellar bar component at $z = 0$, we find that these fractions are very different: 95%, 96% and 92% of stars are born *in-situ* for A-Gadget2, A-Gasoline and B-Gasoline, respectively. These fractions show that a very small percentage of the stars that belong at $z = 0$ to the bar were formed far away from the main progenitor and accreted later on.

Vertical arrows in the top panels in Fig. 9 show bar formation times t_{bar} obtained from Fig. 5. These times seem to correspond approximately with peaks in the star formation times distribution in agreement with previous work from Fanali et al. (2015) pointing out that as the bar forms, the gas reaches the galaxy's most central

regions increasing its star formation rate. Once the bar is formed it takes more time for the gas to reach the central region decreasing the star formation rate. Notice that the t_{bar} also seems to occur near to merger events as seen in Fig. 9. This does not necessarily mean that mergers are the triggers of bar formation but they play an important role on this process. Moetazedian et al. (2017); Zana et al. (2017) study the behaviour of bar formation against tidal interactions produced by mergers and flybys. They concluded that close encounters could delay or accelerate the onset of the bar but do not induce the bar formation.

Accretions events could help to understand the different f_{dec} values obtained for B-Gadget2 ($f_{dec} < 1$ indicating a rising rotation curve) and B-Gasoline ($f_{dec} > 1$ indicating a declining rotation curve; see Fig. 6). Analysing their circular velocity profiles, at the times we chose to calculate f_{dec}, we find that the dark matter halo of B-Gasoline has a slightly declining (nearly flat) profile while B-Gadget2 has a rising one. The rising circular velocity profile of B-Gadget2 seems to be related to its profuse satellite accretion history. Indeed, three massive satellites are accreted and merged at 5.73, 9.45, and 11.88 Gyr, respectively (indicated with magenta vertical arrows in Fig. 9 middle left panel). Moreover, although these satellites produce an abrupt increase in the bar strength parameter ($A_2^{max} > 0.2$), they are followed by a steady decline to $A_2^{max} \sim 0.1$, i.e. well below the adopted value to distinguish between barred and unbarred galaxies (see Fig. 5 solid blue line where the three peaks are prominent). Notice that although three satellites are also seen for B-Gasoline (see Fig. 9 middle right panel) the behaviour of A_2^{max} is steadily increasing with time probably due to their different orbit and mass (e.g. Gerin et al. 1990; Łokas et al. 2016; Peschken & Łokas 2019). Indeed, Zana et al. (2018) argue that the effect of weak interaction could be destructive for the bar formation process. The main difference between B-galaxies seems to come from the strength of the interaction with the 2nd and 3rd satellites and not from the 1st one. At the 1st satellite accretion time ($t \sim 5.6$ Gyr), the stellar mass difference between B-Gadget2 and B-Gasoline main galaxies, or between both 1st satellites, is only about 10%, with this difference increasing up to 40% at redshift $z = 0$. However, the 2nd plus the 3rd satellite have a combined stellar mass of 6.2×10^9 M⊙ and 3.7×10^9 M⊙ for B-Gadget2 and B-Gasoline, respectively, which means that their combined mass is about 70% higher for B-Gadget2 than for B-Gasoline. We consider the combined effect of these two satellites together, given that it is very difficult to disentangle their individual effects on the main galaxy. They accrete approximately at the same time, $t \sim 8$ Gyr, and keep interacting, both between them and with the central galaxy, for at least a couple of Gyrs, before merging at different times. Notice that the B-Gasoline bar can finally develop after the accretion of the 3rd satellite; i.e. after the hectic merger activity has somehow stopped or significantly slowed down. The fact that the "2+3" satellite is much more massive in B-Gadget2 than in Gasoline seems to indicate that the bar formation could have been delayed for a much longer period in B-Gadget2 than in B-Gasoline. Moreover, the last merger event (i.e. the merge of the 3rd satellite) is a much more recent event ($t \sim 12$ Gyr) for B-Gadget2 while it happened much earlier ($t \sim 10.5$ Gyr) for B-Gasoline, giving almost twice as much time for bar development. We would like to stress that many more outputs than those currently available are necessary for CLUES-GASOLINE simulation to enable us to perform a detailed analysis of the tidal interaction effects on these two simulated galaxies.

4   SUMMARY AND CONCLUSIONS

We analyse two zoom-in hydrodynamical numerical simulations of the CLUES project that start at redshift $z = 50$ from identical initial conditions and are evolved with GADGET-2 and GASOLINE codes, respectively. The high-resolution region of the simulated volume is an approximately spherical region of $2h^{-1}$ Mpc radius with about 53 million equal numbers of gas and dark matter particles. At redshift $z = 0$ our simulated galaxies are morphologically classified as discs having from $\sim 250,000$ to $750,000$ star particles inside ($r_{gal} = 0.15 r_{vir}$).

Measuring the radial profile of the normalised amplitude of the $m = 2$ Fourier mode $A_2(R)$ (Eq. 2), we classify our simulated stellar discs as unbarred ($A_2^{max} < 0.2$) or barred ($A_2^{max} > 0.2$). We follow the temporal evolution of our galaxies to study the formation and evolution of the stellar bars. At redshift $z = 0$, the three most massive haloes of each simulation host a central disc galaxy, with half of them (i.e. three) developing a central rotating stellar bar. In the most massive halo, both simulations (CLUES-GADGET2 and CLUES-GASOLINE) develop a bar; in the second massive halo, only the CLUES-GASOLINE simulation shows a bar, and in the third halo, none of them.

With total stellar mass in the range $\sim 0.5 - 1.4 \times 10^{10}$ M , bar length of ~ 1 kpc and pattern speed in the range $32 - 99$ km s^{-1} kpc^{-1} these galaxies compare satisfactorily with observational estimates derived for a sample of barred galaxies by Font et al. (2017); Aguerri et al. (2015) and Corsini (2011). Our bars are short and occupy the short end of the observed bar length distribution, which implies that these high-resolution simulations produce short bars, in contradiction to previous claims that numerical simulations generally produce long bars but infrequently short ones (Erwin 2005). Our bars are short and not so slow in comparison to previous simulations that raised concerns about the overabundance of slow bars in the ΛCDM model. Probably, limited numerical resolution plays a pivotal role in angular momentum transfer between bars and dark matter haloes, artificially reducing their pattern speeds.

We have shown that simulations performed with different codes but starting from identical initial conditions can lead to different bar formation scenarios, because the physics assumed in the simulations can change the final results at small scale where the hydrodynamics of the system prevails over the gravity allowing the bar formation.

In agreement with previous works, bars develop in systems where the disc is gravitationally important compared to the gravitational contribution of the dark matter halo. We have confirmed that f_{disc} or f_{dec} parameters alone are not sufficient to predict bar formation, but combining both, we can efficiently predict that the bar formation process will take place.

After their formation, bars grow in length by a factor between 1-2, while their rotation speeds slow down accordingly. Nevertheless, they are not slow when compared to observed pattern speeds, reducing previous concerns about numerical simulations producing systematically slow bars (Algorry et al. 2017).

Also, we see from the last section that most of the stars that belong to the bar at $z = 0$ are born inside the galaxy and the formation of the bar causes the triggering of star formation, as found in previous works.

DATA AVAILABILITY

The data underlying this article will be shared on reasonable request to the corresponding author.

REFERENCES

Aguerri J. A. L., et al., 2015, A&A, 576, A102
Algorry D. G., et al., 2017, MNRAS, 469, 1054
Athanassoula E., 2003, MNRAS, 341, 1179
Athanassoula E., 2008, MNRAS, 390, L69
Athanassoula E., Misiriotis A., 2002, MNRAS, 330, 35
Athanassoula E., Machado R. E. G., Rodionov S. A., 2013, MNRAS, 429, 1949
Benitez-Llambay A., 2015, py-sphviewer: Py-SPHViewer v1.0.0, doi:10.5281/zenodo.21703, http://dx.doi.org/10.5281/zenodo.21703
Benítez-Llambay A., Navarro J. F., Abadi M. G., Gottlöber S., Yepes G., Hoffman Y., Steinmetz M., 2013, ApJ, 763, L41
Benítez-Llambay A., Navarro J. F., Abadi M. G., Gottlöber S., Yepes G., Hoffman Y., Steinmetz M., 2015, MNRAS, 450, 4207
Bower R. G., Benson A. J., Malbon R., Helly J. C., Frenk C. S., Baugh C. M., Cole S., Lacey C. G., 2006, MNRAS, 370, 645
Cole S., Lacey C. G., Baugh C. M., Frenk C. S., 2000, MNRAS, 319, 168
Combes F., Sanders R. H., 1981, A&A, 96, 164
Combes F., Debbasch F., Friedli D., Pfenniger D., 1990, A&A, 233, 82
Contopoulos G., 1980, A&A, 81, 198
Corsini E. M., 2011, Memorie della Societa Astronomica Italiana Supplementi, 18, 23
Debattista V. P., Sellwood J. A., 2000, ApJ, 543, 704
Efstathiou G., Lake G., Negroponte J., 1982, MNRAS, 199, 1069
Erwin P., 2005, Monthly Notices of the Royal Astronomical Society, 364, 283
Fanali R., Dotti M., Fiacconi D., Haardt F., 2015, MNRAS, 454, 3641
Ferrero I., et al., 2017, MNRAS, 464, 4736
Font J., et al., 2017, ApJ, 835, 279
Fragkoudi F., Grand R. J. J., Pakmor R., Springel V., White S. D. M., Marinacci F., Gomez F. A., Navarro J. F., 2021, A&A, 650, L16
Gerin M., Combes F., Athanassoula E., 1990, A&A, 230, 37
Gottlöber S., Hoffman Y., Yepes G., 2010, arXiv e-prints, p. arXiv:1005.2687
Governato F., et al., 2010, Nature, 463, 203
Guedes J., Callegari S., Madau P., Mayer L., 2011, ApJ, 742, 76
Guo Q., White S., Li C., Boylan-Kolchin M., 2010, MNRAS, 404, 1111
Haardt F., Madau P., 1996, ApJ, 461, 20
Hernquist L., Weinberg M. D., 1992, The Astrophysical Journal, 400, 80
Hockney R. W., Hohl F., 1969, AJ, 74, 1102
Hoffman Y., Ribak E., 1991, ApJ, 380, L5
James R. A., Sellwood J. A., 1978, MNRAS, 182, 331
Kalnajs A. J., 1972, ApJ, 175, 63

Karachentsev I. D., Karachentseva V. E., Huchtmeier W. K., Makarov D. I., 2004, AJ, 127, 2031

Klypin A., Kravtsov A. V., Bullock J. S., Primack J. R., 2001, ApJ, 554, 903

Knebe A., Libeskind N. I., Knollmann S. R., Martinez-Vaquero L. A., Yepes G., Gottlöber S., Hoffman Y., 2011, MNRAS, 412, 529

Knollmann S. R., Knebe A., 2009, ApJS, 182, 608

Lacey C. G., et al., 2016, MNRAS, 462, 3854

Libeskind N. I., Yepes G., Knebe A., Gottlöber S., Hoffman Y., Knollmann S. R., 2010, MNRAS, 401, 1889

Libeskind N. I., Knebe A., Hoffman Y., Gottlöber S., Yepes G., 2011, MN-RAS, 418, 336

Little B., Carlberg R. G., 1991, Monthly Notices of the Royal Astronomical Society, 251, 227

Łokas E. L., Ebrová I., del Pino A., Sybilska A., Athanassoula E., Semczuk M., Gajda G., Fouquet S., 2016, ApJ, 826, 227

Miller R. H., Prendergast K. H., 1968, ApJ, 151, 699

Miller R. H., Prendergast K. H., Quirk W. J., 1970, ApJ, 161, 903

Mo H. J., Mao S., White S. D. M., 1998, MNRAS, 295, 319

Moetazedian R., Just A., 2016, MNRAS, 459, 2905

Moetazedian R., Polyachenko E. V., Berczik P., Just A., 2017, A&A, 604, A75

Mostoghiu R., Di Cintio A., Knebe A., Libeskind N. I., Minchev I., Brook C., 2018, MNRAS, 480, 4455

Okamoto T., Isoe M., Habe A., 2015, PASJ, 67, 63

Ostriker J. P., Peebles P. J. E., 1973, ApJ, 186, 467

Peschken N., Łokas E. L., 2019, MNRAS, 483, 2721

Raiteri C. M., Villata M., Navarro J. F., 1996, A&A, 315, 105

Reiprich T. H., Böhringer H., 2002, ApJ, 567, 716

Sales L. V., Navarro J. F., Schaye J., Dalla Vecchia C., Springel V., Booth C. M., 2010, MNRAS, 409, 1541

Santos-Santos I. M., Brook C. B., Stinson G., Di Cintio A., Wadsley J., Domínguez-Tenreiro R., Gottlöber S., Yepes G., 2016, MNRAS, 455, 476

Santos-Santos I. M. E., Domínguez-Tenreiro R., Granato G. L., Brook C. B., Obreja A., 2017, A&A, 603, A4

Scannapieco C., Athanassoula E., 2012, MNRAS, 425, L10

Sellwood J. A., 2008, ApJ, 679, 379

Sellwood J. A., Debattista V. P., 2006, ApJ, 639, 868

Sellwood J. A., Wilkinson A., 1993, Reports on Progress in Physics, 56, 173

Sparke L. S., Sellwood J. A., 1987, MNRAS, 225, 653

Spergel D. N., et al., 2007, ApJS, 170, 377

Springel V., 2005, MNRAS, 364, 1105

Springel V., Hernquist L., 2003, MNRAS, 339, 289

Stinson G., Seth A., Katz N., Wadsley J., Governato F., Quinn T., 2006, MNRAS, 373, 1074

Tonry J. L., Dressler A., Blakeslee J. P., Ajhar E. A., Fletcher A. B., Luppino G. A., Metzger M. R., Moore C. B., 2001, ApJ, 546, 681

Wadsley J. W., Stadel J., Quinn T., 2004, New Astron., 9, 137

Weinberg M. D., 1985, Monthly Notices of the Royal Astronomical Society, 213, 451

Weinberg M. D., Katz N., 2007a, Monthly Notices of the Royal Astronomical Society, 375, 425

Weinberg M. D., Katz N., 2007b, Monthly Notices of the Royal Astronomical Society, 375, 460

Willick J. A., Courteau S., Faber S. M., Burstein D., Dekel A., Strauss M. A., 1997, ApJS, 109, 333

Yepes G., Gottlöber S., Hoffman Y., 2014, New Astron. Rev., 58, 1

Zana T., Dotti M., Capelo P. R., Bonoli S., Haardt F., Mayer L., Spinoso D., 2017, preprint, (arXiv:1705.02348)

Zana T., Dotti M., Capelo P. R., Mayer L., Haardt F., Shen S., Bonoli S., 2018, MNRAS, 479, 5214

This paper has been typeset from a TEX/LATEX file prepared by the author.